FISEVIER

Contents lists available at ScienceDirect

Atmospheric Environment

journal homepage: www.elsevier.com/locate/atmosenv



Short communication

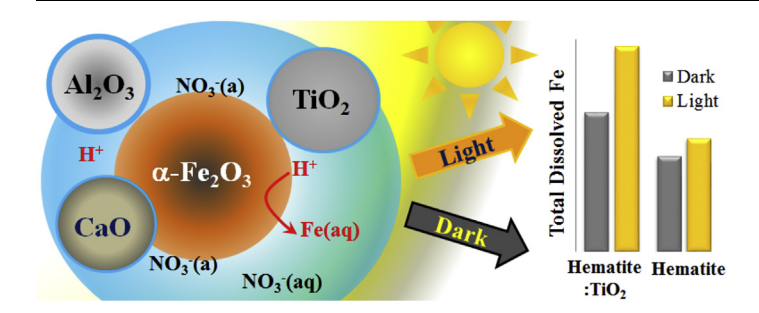
Iron dissolution and speciation in atmospheric mineral dust: Metal-metal synergistic and antagonistic effects



Eshani Hettiarachchi^a, Richard L. Reynolds^{b,c}, Harland L. Goldstein^b, Bruce Moskowitz^c, Gayan Rubasinghege^{a,*}

- ^a Department of Chemistry, New Mexico Institute of Mining and Technology, Socorro, NM, 87801, USA
- ^b U.S. Geological Survey, Denver, CO, 80225, USA

GRAPHICAL ABSTRACT



ARTICLE INFO

Keywords: Bioavailable iron Iron dissolution Photochemistry Mineralogy effects Redox cycling Titanium dioxide

ABSTRACT

Under acidic atmospheric conditions, iron leached from atmospheric mineral dust may influence the distribution of bioavailable iron at a global scale. However, the effects of non-Fe-containing minerals on iron dissolution remain unknown. This work describes metal-metal synergistic and antagonistic effects on iron dissolution that go beyond aggregation and ionic strength effects in mineral dust mixtures. In this study, we investigated iron mobilization by proton-promoted dissolution in natural mineral dust samples from the Kalahari Desert (SZ1) and Australian Red Dawn event (RO), along with one iron oxide proxy, hematite. The total iron dissolution in natural dust samples highly corresponds with the respective amount of Ti, rather than their particle sizes or Fe contents. The dust sample with high Ti content, SZ1, also showed a higher fraction of dissolved Fe(II), under dark conditions. These observations are in good agreement with the dissolution data for hematite artificially mixed with metal oxides. Total iron dissolution in hematite, mixed with TiO_2 , is 1.5- and 2-fold higher compared to that of just hematite under dark and light conditions, respectively. However, dissolution of hematite is suppressed when mixed with TiO_2 compared to that of other mixtures or hematite alone. Yet, dissolved Fe(II) is lower in hematite mixed with TiO_2 under light conditions compared to that of hematite alone, suggesting photo-oxidation of Fe(II) by reactive oxygen species, such as OH radicals.

E-mail addresses: eshani.hettiarachchi@student.nmt.edu (E. Hettiarachchi), rreynolds@usgs.gov (R.L. Reynolds), hgoldstein@usgs.gov (H.L. Goldstein), bmosk@umn.edu (B. Moskowitz), gayan.rubasinghege@nmt.edu (G. Rubasinghege).

^c Institute for Rock Magnetism, Department of Earth Sciences, University of Minnesota, Minneapolis, MN, 55455, USA

^{*} Corresponding author.

1. Introduction

Atmospheric processing of iron-containing mineral dust is important as the primary source of bioavailable iron to ocean life that sequesters carbon via photosynthesis (Cwiertny et al., 2009; Wijenayaka et al., 2012; Lu et al., 2017). Hence, mineral-dust iron both from iron oxides and structural iron such as clay plays a vital role in ocean biogeochemical cycles (Lu et al., 2017). Mineral dust processing in acidicatmospheric environments, i.e. "aging", has been discussed in numerous previous studies, which have shown that the aging process depends on both environmental and particle properties, i.e., pH, solar flux, temperature, acid anions, and particle size (Cwiertny et al., 2008: Hettiarachchi et al., 2018; Journet et al., 2008; Paris et al., 2011; Ravelo-Pérez et al., 2016; Rubasinghege et al., 2010). Given the complexity of mineral-dust composition, Fe-bearing minerals are wellmixed with non-Fe-containing metal oxides (Elzinga et al., 2011). To our knowledge, however, the potential effects of non-Fe-containing minerals on iron dissolution have not been studied thoroughly, and hence these effects remain largely unknown. In this study, using both natural dusts and mineral-dust proxies, the synergistic and antagonistic effects of three common phases on iron dissolution are explored. Because particle aggregation is known to quench dissolution, we have investigated effects that go beyond ionic strength and particle aggregation (Rubasinghege et al., 2012). Additionally, the role of solar radiation in these synergistic effects is investigated.

Atmospheric processing of Fe-containing mineral dust and subsequent iron dissolution occur by three main mechanisms: proton-promoted, ligand-controlled, and reductive-dissolution. All these mechanisms involve adsorption of acid anions or organic ligands onto Fecontaining mineral surfaces followed by detachment of iron (Wiederhold et al., 2006; Rubasinghege et al., 2010). Mineral dust typically consists of large amounts of other non-Fe-containing minerals, originating both from natural and anthropogenic sources, which may also compete for acid anions and/or organic ligands, and thus may affect iron dissolution. Moreover, different products formed during the reactions, from other minerals can modify surfaces by activation, passivation, or crystal-face alterations, thereby affecting overall processing and iron dissolution in mineral dust (Grybos et al., 2010; Henderson, 2011). Therefore, understanding the synergistic effects of non-Fe-containing minerals on Fe mobilization is important to accurately model bioavailable iron production for ocean life. The current study is intended to lessen the discrepancies between the field and laboratory observations, and atmospheric modeling studies on bioavailable Fe leaching from mineral dusts (Doney et al., 2001; Held, 2005; Lohmann et al., 2007; Jackson and Burd, 2015).

Previous studies have shown that the amount of soluble iron in aerosol mineral dusts does not necessarily correlate with their total iron content or particle surface area and that the mineralogy of iron-containing minerals also appears to be a critical factor (Cwiertny et al., 2008; Journet et al., 2008; Fu et al., 2010; Hettiarachchi et al., 2018). Fu et al. (2010), reported that Fe-containing Arizona Test Dust (AZTD) particles were more soluble than Inland Saudi Sand (IS) and Saharan Sand (SS) regardless of experimental conditions. They further discussed that the AZTD contained relatively higher content of clay minerals, whereas the IS and SS were rich in unreactive quartz sand. Therefore, other minerals in the mineral dust might affect the extent of acid mobilization of iron. The various minerals in the dust may leach different cations and anions to the deliquescent layer, altering the surface chemistry, including redox cycling, acid-base reactions, and photo-reduction. These changes would ultimately initiate different reaction pathways that influence the rate and extent of iron dissolution and speciation. The discrepancies observed between field and laboratory results relative to model studies could be caused by the incapacity of simplistic models to account for these synergistic and antagonistic effects (Doney et al., 2001; Held, 2005; Lohmann et al., 2007; Jackson and Burd, 2015).

Here, we present the differences in iron dissolutions from two natural dusts that contain similar amounts of iron and the possible mineralogical effects on other non-Fe-containing minerals in the dust mixture. The iron dissolution experiments were performed in solutions of 0.01 M nitric acid (pH 2), conditions specifically chosen to mimic the low pH environments in the acidic deliquesce layer of mineral dust, as proposed by numerous previous investigators (Cwiertny et al., 2008; Rubasinghege et al., 2010; Fu et al., 2010; Borgatta et al., 2016; Hettiarachchi et al., 2018). These synergistic and antagonistic effects are further supported by studies done on the dissolution of α-Fe₂O₃ (hematite), a widely abundant single-component iron oxide in mineral dust, in the presence of three common metal-oxides- TiO₂ (anatase), y-Al₂O₃ (alumina), and CaO (calcium oxide)- that originate from both natural and anthropogenic processes (Krueger et al., 2004; Kandler et al., 2007; Shao et al., 2007; Ma et al., 2013; Mallampati et al., 2018; Tabesh et al., 2018). Albeit the natural abundance of CaO is would likely be lower than that of CaCO₃ in mineral dusts due the reactivity of CaO with CO2, the former was selected to avoid the complexity of having two competitive anions (nitrate and carbonate) in a reaction mixture. Such a mixture would produce large differences in reactions driven by ligand-controlled mechanism. In general, due to both natural and anthropogenic sources, mineral dust aerosol may contain relatively high amounts of these selected metal oxides in comparison to hematite, where these distributions changes seasonally (Krueger et al., 2004; Kandler et al., 2007; Chen et al., 2012). Therefore, in the current work, the molar ratio of hematite to other oxides was selected to be 1:3. Further, to highlight the fact the interactions among minerals are mainly limited to surface and solution-phase reactions, and not to internal mixing of their lattice structures, these mixtures are referred to as "externally-mixed" minerals.

2. Materials and methods

2.1. Natural dust samples

Sample SZ1 was collected from the top 5 cm of a sand dune in the Kalahari Desert, Botswana, Africa (-26.72, 20.65) (Bhattachan et al., 2012). The bulk sample was sieved to produce a < 45-micrometer fraction. The Rawson Orange (RO) dust sample was swept up from a flat uncovered surface at Orange NSW, Australia (-33.2844, 149.0259) one day after having been deposited by the Red Dawn dust storm (Reynolds et al., 2014).

2.2. Materials

All chemicals were reagent grade or better and used as received. The dissolution studies were done using common mineral dust proxies, i.e., hematite (α-Fe₂O₃, US Research Nanomaterials, 99.5%), alumina (γ-Al₂O₃, Degussa, +98%), anatase (TiO₂, Degussa, 99%), and calcium oxide (CaO, Sigma Aldrich, 99.9%) following a well-established procedure (Rubasinghege et al., 2010; Borgatta et al., 2016; Hettiarachchi et al., 2018). All the solutions were prepared in Milli-Q water (18 $M\Omega$, Milli-Q Advance 10). Hydroxylamine hydrochloride (NH2:OH:HCl, Acros Organics, 99%), ammonium fluoride (NH₄F, Baker Chemicals, 99%), concentrated hydrochloric acid (HCl, SchoIAR chemicals, 36%), ammonium acetate (CH3COONH4, Mallinckrodt, 99%), acetic acid (CH₃COOH, VWR International, glacial), 1,10-phenanthroline (C₁₂H₈N₂, Acros organics, 99+%), and ferrous ammonium sulfate hexahydrate (Fe(NH₄)₂(SO₄)₂·6H₂O, Fischer Scientific, 98.5%) were used during the analysis of dissolved iron based on the procedure previously described in Stucki, 1981.

2.3. Methods

2.3.1. Particle characterization

The shape and size of mineral particles were determined from single particle analysis with scanning electron microscope (SEM) and

transmission electron microscope (TEM). The size distribution was determined by analyzing $\sim\!800$ particles using the software package ImageJ. Surface areas of mineral samples were measured in a seven-point $N_2\text{-Brunauer-Emmet-Teller}$ (BET) surface area analyzer. In BET analysis, the samples were outgassed overnight ($\sim\!24\,\text{h})$ at a temperature of 105 °C prior to the BET analysis.

Major, minor, and trace elements of the dust samples were determined using inductively coupled plasma - atomic emission spectroscopy (ICP-AES) following a 4-acid digestion method (Briggs, 2002). Fecontaining solid phases were identified using reflectance spectroscopy and Mössbauer spectroscopy.

2.3.2. Batch reactor studies - iron dissolution

Batch reactor studies were carried out to simulate iron leaching from aerosol dust particles in the presence of an acid deliquesce layer where the pH could be as low as 1 or 2 (Cwiertny et al., 2008). As previously reported, the conditions in the acidic deliquesce layer were simulated in custom-built glass reactors (Borgatta et al., 2016; Cwiertny et al., 2008; Fu et al., 2010; Hettiarachchi et al., 2018; Rubasinghege et al., 2010). The reaction vessel has a suspension capacity of 100 mL and a removable airtight top. In both natural dust and proxies, the particle loading was 0.2 g/L of mineral dust in nitric acid solutions at pH 2. In the experiment with dust proxies, hematite was mixed with a non-iron-containing metal oxide, i.e., anatase, alumina, or calcium oxide. Prior to the dissolution experiment, the acid solution was purged with nitrogen gas at 5 sccm for 5 min to obtain a reduced and oxygenfree atmosphere. The solution was agitated constantly to mimic the mixing in the deliquescence layer. These experiments were performed in the absence and presence of a solar simulator (150 W xenon lamp, Newport Corp Sol1A ABB). A quartz window (12.5 cm²) mounted on the top of the reaction vessel permitted light entry during the solar experiments. Dark experiments were carried out in a custom-designed dark room without any stray light. The glass reactor is also equipped with a temperature probe, a standardized pH electrode, and conductivity probe to measure these parameters throughout the dissolution experiment. The temperature was kept constant at 25 °C using a water jacket. The suspension samples were periodically removed from the reactor using a disposable syringe that was connected to 12 cm of Teflon tubing. The collected samples were filtered through $0.2\,\mu m$ pore size filters and analyzed using the 1,10-phenanthroline method (Stucki, 1981). Prior to filtration, the samples were centrifuged to ensure no particles in the filtrate. Control experiments verified that no dissolved iron originated from the non-Fe-containing phases.

2.3.3. Statistical analysis

All of the dissolution experiments were conducted in three independent experiments (triplicated) and average measurements are reported. Reported errors represent one standard deviation. Paired ttests at 95% confidence level were performed to identify the variations among different experiments, using MINITAB 17. Variations among samples in elemental composition were identified using ANOVA. Unless otherwise reported, these variations were considered significant when p-value < 0.05.

3. Results and discussion

3.1. Particle characterization

The size distribution, determined from SEM and TEM images, revealed that these particles range from nanoscale to microscale. Hematite, TiO₂, Al₂O₃, and CaO particle sizes were 32 (\pm 2) nm, 25 (\pm 3) nm, 13(\pm 2) nm, and 82(\pm 16) nm, respectively. The particle sizes of SZ1 and RO ranged between 1 and 45 µm. The specific surface areas of the samples were 100(\pm 4) m^2g^{-1} , 59(\pm 2) m^2g^{-1} , 154(\pm 3) m^2g^{-1} , and 37(\pm 5) m^2g^{-1} for hematite, TiO₂, Al₂O₃, and CaO,

Table 1Major elemental composition of natural dust samples as derived from ICP-AES analysis.

| Sample | %Al | %Ca | %Fe | %Ti |
|--------------------|------|------|------|-------|
| SZ1 | 5.88 | 1.99 | 4.82 | 1.31 |
| Rawson Orange (RO) | 8.52 | 1.16 | 4.84 | 0.474 |

respectively. Those of SZ1 and RO were respectively $8.5(\pm 1)~\text{m}^2\text{g}^{-1}$ and $59.6(\pm 4.4)~\text{m}^2\text{g}^{-1}$. Whereas smaller particles generally contribute to higher surface areas, several other factors, such as porosity, specific active sites, and exposed crystal planes, could also influence the surface area available for reactions. Particles that are more porous show higher surface areas than their non-porous counterparts do. Given the differences in the location and origin of these two samples, it is thus possible to have such a difference in specific surface areas.

Both SZ1 and RO (Reynolds et al., 2014) contained hematite and trace amounts of goethite and magnetite as Fe-oxide containing solid phases. Mössbauer analysis indicates that hematite accounts for 52% and 43% of the total Fe, whereas magnetite accounts for 1.5% and 0.9% in SZ1 and RO, respectively. The remaining Fe occurs in other Fecontaining mineral phases such as clay. The elemental percentages of the SZ1 and RO samples are listed in Table 1. The two samples contain almost the same amount of iron by weight.

3.2. Mineralogy and iron dissolution in atmospheric aerosol dust

The effects of non-Fe-containing metal oxides on iron dissolution and speciation were investigated using two natural dust samples. These samples were specifically selected due to their similar Fe content (p > 0.05) and significant variation in amount of Ti (p < 0.07). (Table 1). Comparisons of total iron dissolution and Fe(II) for SZ1 and RO samples are shown in Fig. 1. On mass basis, total iron dissolution for SZ1 was $\sim\!2.5$ -fold higher compared to RO, despite their similar Fe content (Fig. 1(a)). The pseudo-first order rates, derived from the Langmuir model, were 55 \pm 3 μ M g $^{-1}$ hr $^{-1}$ and 20 \pm 2 μ M g $^{-1}$ hr $^{-1}$ for SZ1 and RO, respectively. However, to eliminate the effects arising from surface area, these results were normalized to their respective areas.

Under dark conditions, the percentage of dissolved Fe(II) (=([dissolved Fe(II)]/[total dissolved Fe]) \times 100%) of SZ1 and RO were respectively 51% and 40%, whereas under light conditions they were respectively 27% and 73% for SZ1 and RO, indicating a decrease in dissolved Fe(II) fraction for SZ1, but an enhancement for RO. From these results, therefore, it is clear that having a similar amount of Fe and phase composition does not necessarily yield similar dissolved iron dissolution and speciation. The extent of dissolution can differ greatly, and these differences can be attributed to the variations in other metal oxides. Moreover, structural iron (Fe from non-iron oxides, such as clays) accounts for a substantial amount of iron in mineral dust (Lu et al., 2017; Zhao et al., 2018). Thus, variations in the percentages of clay-mineral compositions may also contribute to the Fe dissolved.

Experimental evidence on single-component minerals has demonstrated that iron is variably leached from different Fe-bearing minerals (Journet et al., 2008). However, many other non-Fe-containing minerals can apparently have very strong influence on the extents of iron dissolution. As shown in Table 1, the two natural samples differ greatly in amounts of Al, Ca, and Ti. These elements generally exist in mineral dust as oxides and carbonate minerals (Krueger et al., 2004; Kandler et al., 2007; Chen et al., 2012). To investigate whether the above differences arose from differences in chemistry, we explored hematite dissolution in the presence of Al_2O_3 , CaO, and TiO_2 .

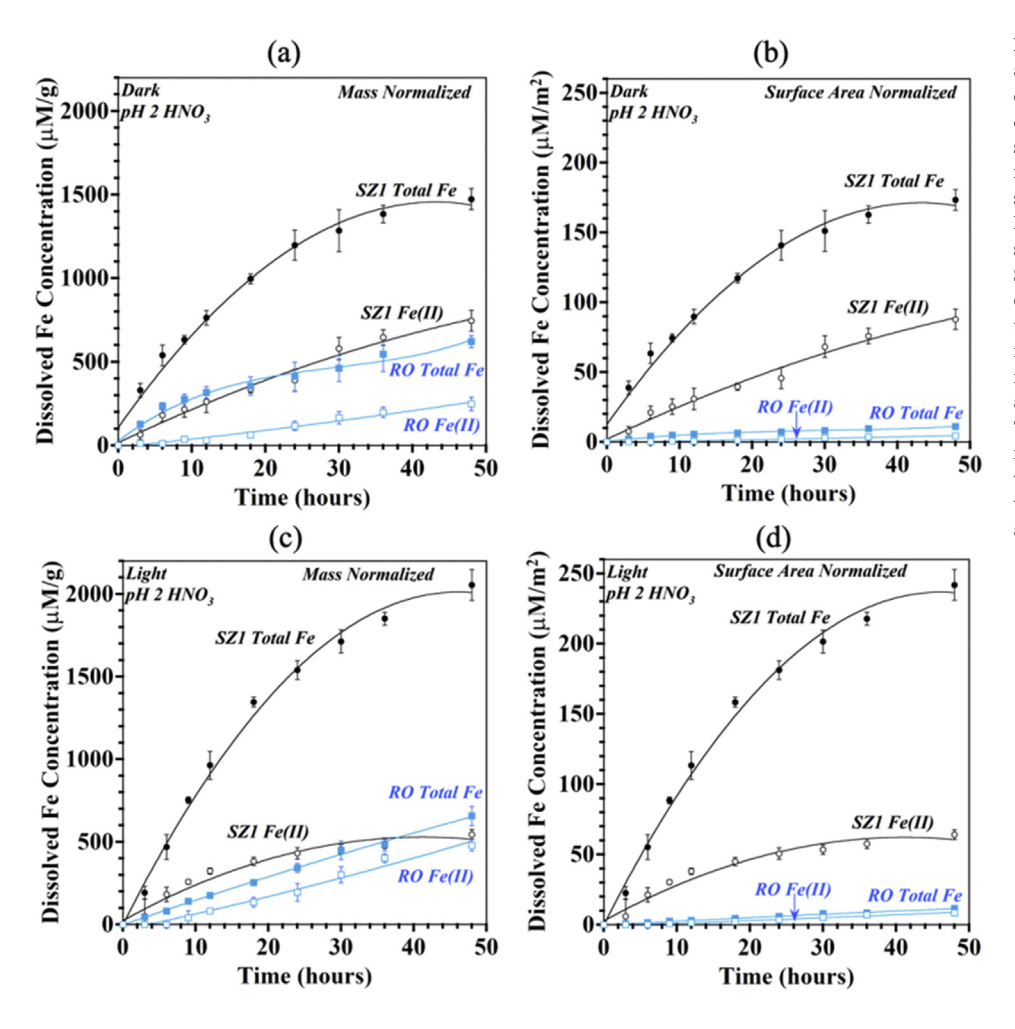


Fig. 1. The extents of iron dissolutions from SZ1 and RO at pH 2 nitric acid in dark and light conditions. Dissolved total iron and Fe(II) (a) in the dark on mass normalized basis (b) in dark on surface area normalized basis (c) in the light, on mass normalized basis, and (d) in the light, on surface area normalized basis. Data are fitted to Langmuir model surface areas (Fig. 1(b)). On surface area basis, the total iron dissolution from SZ1 is ~16-fold higher than RO under the same conditions. Upon simulated solar irradiation, both the dust samples showed enhancement in total iron dissolution, (Fig. 1(c) and (d)). The pseudo first order rates of total iron dissolution from SZ1 and RO under light at pH 2 nitric acid were $75 \pm 5 \,\mu\text{M g}^{-1}\text{hr}^{-1}$ and $14 \pm 3 \,\mu\text{M g}^{-1}\text{hr}^{-1}$, respectively. Under light conditions, iron in SZ1 was ~3-fold more soluble than RO on mass basis whereas it was ~21-fold more soluble on surface area basis.

3.3. Hematite dissolution in the presence of other oxides

3.3.1. Iron dissolution under dark conditions

Our results highlight significant variations in the rate and extent of iron dissolution for different mixtures of mineral oxides indicated in Fig. 2, which compares total dissolved Fe and dissolved Fe(II) for these mixtures at pH 2 in the dark. According to Fig. 2(a), TiO₂ enhances iron dissolution in hematite, whereas Al₂O₃ and CaO quench the process. The total dissolved Fe for the hematite:TiO₂ mixture after 48 h was at

least 1.6-fold higher compared to that of hematite alone. However, hematite:Al $_2O_3$ and hematite:CaO mixtures showed about 1.5- and 6-fold decrease, respectively, in their total iron dissolution compared to just hematite after the same elapsed time. The initial rates of total iron dissolution were $117(\pm\,3)~\mu\text{Mg}^{-1}\text{hr}^{-1},~115(\pm\,2)~\mu\text{Mg}^{-1}\text{hr}^{-1},~82(\pm\,2)~\mu\text{M.g}^{-1}\text{hr}^{-1},~and~30(\pm\,1)~\mu\text{Mg}^{-1}\text{hr}^{-1}$ for hematite and hematite in the presence of TiO $_2$, Al $_2O_3$, and CaO mixtures, respectively. Thus, during the first 20 h of dissolution, no significant difference was observed between hematite and the hematite:TiO $_2$ mixture. These

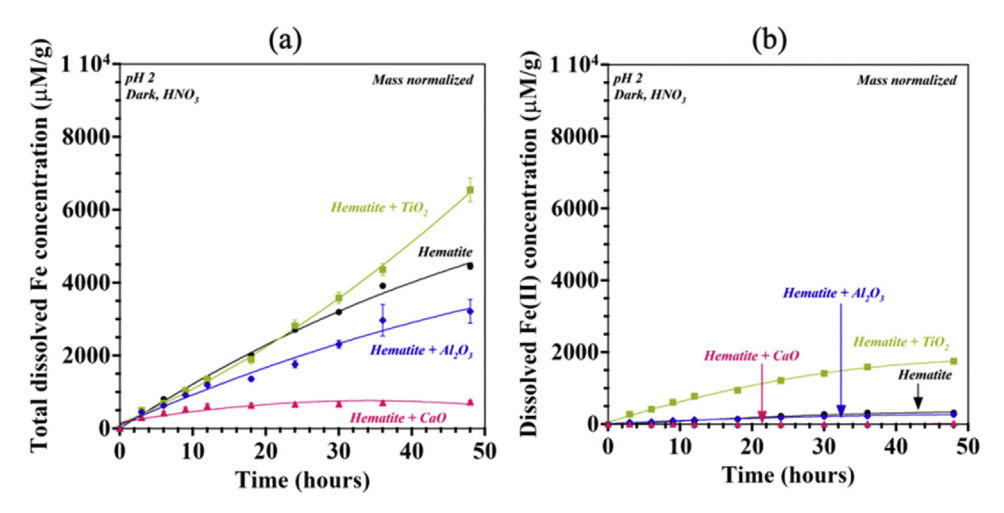


Fig. 2. A comparison of (a) total iron dissolution, (b) dissolved Fe(II) concentration, in hematite mixed with various metal oxides (Al₂O₃, TiO₂ and CaO) at pH 2. The data presented are normalized to the initial mass of hematite.

results suggest that the iron dissolution of hematite is enhanced in atmospherically processed, hence "aged", particles in the presence of ${\rm TiO_2}$ under dark conditions. Similar to total dissolved iron, the highest dissolved Fe(II) fraction was also recorded in the hematite: ${\rm TiO_2}$ mixture. Dissolved Fe(II) concentration in hematite: ${\rm TiO_2}$ was at least 5-fold higher than that of hematite alone (Fig. 2(b)).

The observed differences in iron dissolution may be attributed to several factors that govern surface processes. Ionic strength plays a vital role in particle aggregation, thereby decreasing the surface area available for dissolution reactions (Rubasinghege et al., 2012). In this study, the ionic strengths of reaction mixtures were calculated using electrical conductivity measurements and a method first described by Grifin and Jurinak, which was later adopted by many researchers (Sarkar, 2005: Chesworth, 2008). These data are provided in Supporting Information along with iron dissolution measurements, normalized to their respective ionic strengths. No large differences in ionic strength were observed possibly due to the larger contribution from nitric acid in the medium. Moreover, in the normalized data for ionic strength, the previously described effects of TiO2, Al2O3, and CaO on hematite dissolution remained evident. Thus, our results highlight synergistic and antagonistic effects in externally mixed mineral oxides that go beyond ionic strength effects.

Heterogeneous uptake of acidic gases and water vapor onto mineral dust yields a deliquescent layer with low pH (Rubasinghege et al., 2010). However, it is well known that the pH of this deliquescent layer depends on acid-base properties of the mineral-dust mixture as the adsorbed acid is first titrated by the basic minerals (Goodman et al., 2001; Rubasinghege et al., 2010; Nenes et al., 2011). As previously reported by Goodman et al. (2001) the increasing order of basicity of the selected oxides is $Al_2O_3 < TiO_2 < CaO$, although the first two are amphoteric in nature while the last one is basic. Thus, the solution pH is also expected to vary in a similar order when hematite is mixed with these mineral oxides as shown in Fig. 3 as a function of reaction time.

Our results indicate that the solution pH was always well below 3. Consequently, Fe(III) will stay soluble, as it precipitates only when the solution pH exceeds 4 (Brezonik and Arnold, 2011). For hematite:TiO₂, it is also noteworthy that pH greatly decreases with the reaction time, whereas pH either increases or remains almost the same for other mixtures. Therefore, we propose that the increase of acidity in hematite:TiO₂, in whole or in part, could be the reason for the observed enhancement in iron dissolution under these conditions as proton-promoted dissolution is dominant at low pH conditions. A similar trend in pH variation occurred for SZ1 under dark conditions (Fig. S3), indicating a similar relation between pH and Ti concentration. However,

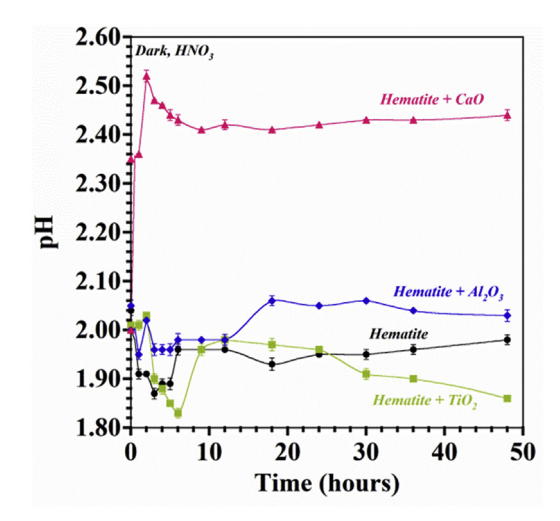


Fig. 3. Variation of solution pH of over time in the presence of nitric acid medium in dark. Initial pH of the solution was 2.00.

the mechanisms behind the unique behavior of TiO₂ as seen in these experiments are still unknown and further research is suggested.

For all four reaction systems, dissolved Fe(II) under dark conditions is shown in Fig. 2(b). Many iron oxides, including hematite, contain surface defects where Fe(III) and Fe(II) oxidation states are present in different ratios (Henderson, 2003; Yamashita and Hayes, 2008). The dissolved Fe(II) fractions were 7%, 9%, and 3% in hematite, hematite:Al $_2$ O $_3$, and hematite:CaO, respectively possibly due to these defects. However, the dissolved Fe(II) was \sim 27% for hematite:TiO $_2$, indicating Fe(III) reduction in the reaction medium. It was previously reported that Ti(III) surface defects (TSDs), found on TiO $_2$ surfaces, can be readily oxidized if an oxidizing agent is encountered (Xiong et al., 2012). Perhaps TSDs play a role in reducing dissolved Fe(III) to Fe(II), thereby increasing the dissolved Fe(II) fraction. Having nitrate in the medium, these redox reactions have the potential to proceed through surface adsorbed nitrate. Further research is required to investigate these mechanisms.

3.3.2. The effect of solar radiation

Previous studies have shown that iron dissolution can either increase or decrease upon irradiation depending on the reaction environment, i.e., acid anions and the mineral itself. Fu et al. (2010) reported that AZTD has higher total iron dissolution under light in the presence of HCl and HNO₃, but iron dissolution diminishes in the presence of H₂SO₄. However, the total iron dissolution from goethite (α -FeOOH) increases under light conditions regardless of the acid, i.e., HCl, H₂SO₄ or HNO₃ (Rubasinghege et al., 2010). These findings suggest that the influence of solar radiation greatly depends on the mineralogy of Fe-containing particles.

Iron dissolution was compared among different mixtures of hematite under light conditions. (Fig. 4). The extent of total iron dissolution in hematite:TiO $_2$ is about 2-fold higher than that of just hematite under the same conditions (Fig. 4(a)). In comparison to the dark condition, more iron dissolved in the presence of TiO $_2$ under light. Moreover, these differences were apparent during the early stage of the reaction. However, the total iron dissolution in CaO and Al $_2$ O $_3$ mixtures showed no significant difference between dark and light conditions. The rates of total iron dissolution under these conditions were $106(\pm3)~\mu Mg^{-1}hr^{-1},~200(\pm2)~\mu Mg^{-1}hr^{-1},~76(\pm2)~\mu Mg^{-1}hr^{-1},~and 78(\pm3)~\mu Mg^{-1}hr^{-1}$ for hematite, hematite:TiO $_2$, hematite:Al $_2$ O $_3$, and hematite: CaO, respectively. These results suggest that in the presence of solar radiation, semiconductor minerals in the mixture could initiate additional photochemical reaction pathways that go beyond lowering the pH of the reaction medium.

In photo-reductive dissolution, Fe(III) is reduced to Fe(II) by photoexcited electrons, a process that enhances the total iron dissolution (Fu et al., 2010; Rubasinghege et al., 2010). Nevertheless, the exact role of TiO₂ in photo-reductive iron dissolution, in externally mixed Fe-containing aerosols, is still unknown. Previously, Xiong et al. (2012) reported that TSDs form extensively upon irradiation. On the other hand, TiO2 is known to catalyze photochemical production of hydroxyl radicals (OH·) in aqueous solutions. By reacting with HNO₃ or NO₃, OH· can further generate other reactive oxygen species (ROS), which may enhance iron dissolution (Brown et al., 2001; Nakamura and Nakato, 2004; Shkrob et al., 2011). In addition, adsorbed nitrates as chromopores can further influence photochemical reaction pathways and thus enhance the total Fe dissolution (Nanayakkara et al., 2014; Hettiarachchi et al., 2018). Hence, we postulate that photochemical and redox coupling reactions, at least in part, enhance the dissolution of hematite in the presence of TiO2 and solar flux.

In contrast to higher total iron production in hematite:TiO₂, the dissolved Fe(II) is slightly lower compared to that of hematite (Fig. 4(b)). The photo-generated OH· can readily oxidize Fe(II) to Fe (III), thereby reducing the overall dissolved Fe(II) fraction according to Eq. (1) (Brown et al., 2001; Nakamura and Nakato, 2004; Shkrob et al., 2011; Silveira et al., 2017; Hettiarachchi et al., 2018).

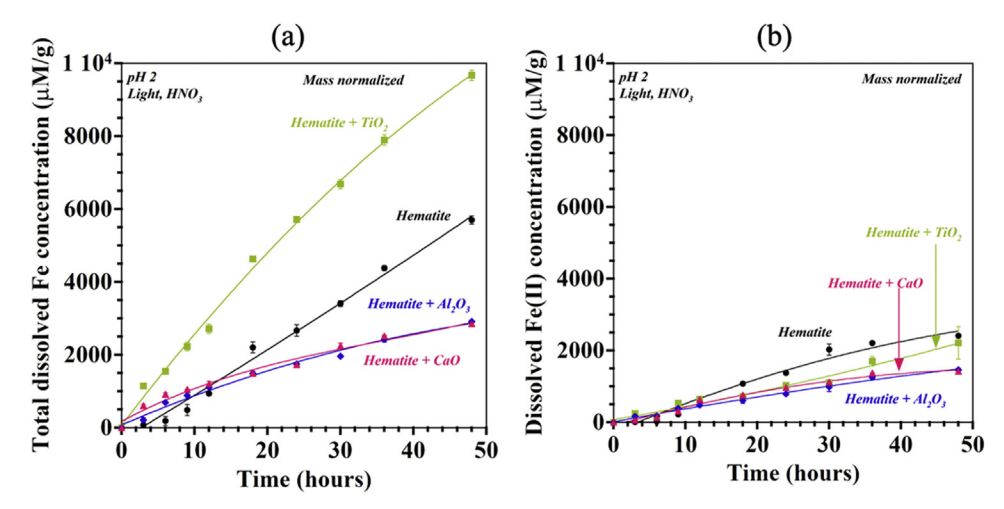


Fig. 4. A comparison of (a) total iron dissolution, (b) dissolved Fe(II) concentration, in hematite mixed with various metal oxides (Al_2O_3 , TiO_2 , and CaO) at pH 2 in the presence of solar radiation. The data presented are normalized to the mass of hematite.

$$Fe(II) + OH \rightarrow Fe(III) + OH$$
 (1)

Therefore, the observed depletion of the dissolved Fe(II) fraction from SZ1 upon irradiation compared to its dark counterpart can be due to the effect arising from its high Ti content.

4. Conclusion

The current study used mineral dust proxies' hematite, TiO₂, Al₂O₃, and CaO to explain some of the iron dissolution trends observed in two different mineral dust samples collected from Australia (RO) and Kalahari Desert (SZ1). Our results primarily highlight that mineral dusts with elevated %Ti show enhanced total iron dissolution, regardless of the availability of solar light. However, the presence of Ti decreases the dissolved Fe(II) fraction in solution upon irradiation. Our studies with hematite, used commonly to replicate dust properties in laboratory experiments, revealed for the first time interesting synergistic and antagonistic effects on iron dissolution, explaining the above observations in natural dusts. The extent of total iron dissolution in hematite increases when mixed with TiO2, under both dark and light conditions. In the dark conditions, lowering pH in the reaction medium facilitates the enhanced iron dissolution. The enhancement is more prominent under light conditions and is found even at early stages of the reaction. These results suggest additional photochemical reaction pathways in the presence of TiO2 and light. In contrast, the mixtures of Al2O3 or CaO with hematite diminish iron dissolution in hematite, especially with CaO, under both dark and light conditions at pH 2. These observations could be attributed to the increased pH due to their inherent basicity. Also, it is noteworthy that in the presence of CaO, solution-phase reactions involving Ca2+ could also occur along with the surface reactions.

In the dark, the increase in dissolved Fe(II) fraction in hematite when mixed with TiO₂, is possibly due to Fe(III) reduction, possibly initiated by Ti(III) surface defects. Under light conditions, however, the fraction of dissolved Fe(II) is slightly lower due to the oxidation by OH-that formed during the photo-cleavage of adsorbed water on TiO₂. The observation that externally-mixed TiO₂ (anatase) showed an important effect on hematite dissolution suggests further experiments with other Ti-containing mineral phases, including rutile. Moreover, these studies could be extended to determine the effects that arise from just elemental Ti and the photo-catalytic activity of TiO₂. Also worthy of study would be to ascertain how the incorporation of radicals and electron scavengers might control radical-mediated reaction pathways and mechanisms under light conditions. Finally, further research is needed to better understand the synergistic effects of non-Fe-containing minerals

on bioavailable iron production and oceanic iron fertilization.

Previous studies reported high amounts of TiO2 (both rutile and anatase) and ilmenite in Saharan and Southern Ocean dust (Kandler et al., 2007; Chen et al., 2012; Ingall et al., 2018). In Saharan dust, TiO₂ can be as high as 4.5% (Chen et al., 2012). In a recent field study on Fe solubility of dust aerosols, Ingall et al. (2018) reported that there was no direct correlation between Fe solubility and total Fe content or oxidation state of Fe. However, their mineralogical studies suggested that the dust samples with greater solubilized iron, collected at Southern Ocean and Finokalia research stations from Saharan air masses, contained higher amount of ilmenite, FeTiO3. Furthermore, in a good agreement with our findings, Fu et al. (2010) previously reported higher total dissolved iron and lower Fe(II) concentrations for source materials of Inland Saudi Sands and Saharan Sands upon exposure to the light. In contrast, Arizona Test Dust, with a lower amount of Ti, showed an increase in Fe(II) concentration under the same conditions. Although authors attributed these differences to the overall mineralogy, we propose that differences in their Ti amounts may play a major role. Therefore, understanding and then introducing these effects to the biogeochemical models may diminish the discrepancies between observations and predictions in field and laboratory settings.

Acknowledgment

This research did not receive any specific grant from funding agencies in the public, commercial, or not-for-profit sectors. The authors thank the Department of Chemistry, New Mexico Institute of Mining and Technology. The Institute for Rock Magnetism (IRM) is supported by the Instruments and Facilities Program of the NSF Division of Earth Science. This is IRM contribution 1801.

The authors are grateful to Paolo D'Odorico and Abi Bhattachan for providing the Kalhari sample, to Stephen Cattle for providing the Australian sample, and to Ray Kokaly for determining iron phases from reflectance spectroscopy. This research was supported in part by the Climate and Land Use Change Program of the U.S. Geological Survey. Any use of trade, product, or firm names is for descriptive purposes only and does not imply endorsement by the U.S. Government. The authors also thank George Breit for his thorough and insightful review which greatly improved this manuscript.

Appendix A. Supplementary data

Supplementary data related to this article can be found at http://dx.doi.org/10.1016/j.atmosenv.2018.06.010.

References

- Bhattachan, A., D'Odorico, P., Baddock, M.C., Zobeck, T.M., Okin, G.S., Cassar, N., 2012. The Southern Kalahari: a potential new dust source in the Southern Hemisphere? Environ. Res. Lett. 7, 024001. http://dx.doi.org/10.1088/1748-9326/7/2/024001.
- Borgatta, J., Paskavitz, A., Kim, D., Navea, J.G., 2016. Comparative evaluation of iron leach from different sources of fly ash under atmospherically relevant conditions. Environ. Chem. https://doi.org/10.1071/EN16046.
- Brezonik, P.L., Arnold, W.A., 2011. Water Chemistry.
- Briggs, P.H., 2002. The determination of forty elements in geological and botanical samples by inductively coupled plasma-atomic emission spectrometry. In: Taggart Jr.J.E. (Ed.), Analytical Methods for Chemical Analysis of Geologic and Other Materials, pp. I1–I14 U.S. Geological Survey Open-File Report 02–223.
- Brown, S.S., Burkholder, J.B., Talukdar, R.K., Ravishankara, A.R., 2001. Reaction of hydroxyl radical with nitric Acid: insights into its mechanism. J. Phys. Chem. A 105, 1605–1614. https://doi.org/10.1021/jp002394m.
- Chen, H., Nanayakkara, C.E., Grassian, V.H., 2012. Titanium dioxide photocatalysis in atmospheric chemistry. Chem. Rev. https://doi.org/10.1021/cr3002092.
- Chesworth, W., 2008. Encyclopedia of Soil Science.
- Cwiertny, D.M., Baltrusaitis, J., Hunter, G.J., Laskin, A., Scherer, M.M., Grassian, V.H., 2008. Characterization and acid-mobilization study of iron-containing mineral dust source materials. J. Geophys. Res. Atmos. 113. https://doi.org/10.1029/ 2007.JD009332.
- Cwiertny, D.M., Hunter, G.J., Pettibone, J.M., Scherer, M.M., Grassian, V.H., 2009. Surface chemistry and dissolution of alpha-FeOOH nanorods and microrods: environmental implications of size-dependent interactions with oxalate. J. Phys. Chem. C 113, 2175–2186. https://doi.org/10.1021/jp807336t.
- Doney, S.C., Lima, I., Lindsay, K., Moore, J.K., Dutkiewicz, S., Friedrichs, M.A.M., Matear, R.J., 2001. Marine biogeochemical modeling: recent advances and future challenges. Oceanography 14, 93–107.
- Elzinga, E.J., Gao, Y., Fitts, J.P., Tappero, R., 2011. Iron speciation in urban dust. Atmos. Environ. https://doi.org/10.1016/j.atmosenv.2011.05.042.
- Fu, H., Cwiertny, D.M., Carmichael, G.R., Scherer, M.M., Grassian, V.H., 2010. Photoreductive dissolution of Fe-containing mineral dust particles in acidic media. J. Geophys. Res. Atmos. 115. https://doi.org/10.1029/2009JD012702.
- Goodman, A.L., Bernard, E.T., Grassian, V.H., 2001. Spectroscopic study of nitric acid and water adsorption on oxide particles: enhanced nitric acid uptake kinetics in the presence of adsorbed water. J. Phys. Chem. A 105, 6443–6457. https://doi.org/10. 1021/ip0037221.
- Grybos, M., Michot, L.J., Skiba, M., Billard, P., Mustin, C., 2010. Dissolution of anisotropic colloidal mineral particles: evidence for basal surface reactivity of nontronite. J. Colloid Interface Sci. 343, 433–438. https://doi.org/10.1016/j.jcis.2009.11.058.
- Held, I.M., 2005. The gap between simulation and understanding in climate modeling. Bull. Am. Meteorol. Soc. 1609–1614. https://doi.org/10.1175/BAMS-86-11-1609.
- Henderson, M.A., 2003. Surface stabilization of organics on hematite by conversion from terminal to bridging adsorption structures. Geochem. Cosmochim. Acta 67, 1055–1063. https://doi.org/10.1016/S0016-7037(02)00884-0.
- Henderson, M.A., 2011. Surface chemistry of trimethyl phosphate on α -Fe₂O₃. J. Phys. Chem. C 115, 23527–23534. https://doi.org/10.1021/jp208978d.
- Hettiarachchi, E., Hurab, O., Rubasinghege, G., 2018. Atmospheric processing and iron mobilization of ilmenite: iron- containing ternary oxide in mineral dust aerosol. J. Phys. Chem. C Articles ASAP. https://doi.org/10.1021/acs.jpca.7b11320.
- Ingall, E.D., Feng, Y., Longo, A.F., Lai, B., Shelley, R.U., Landing, W.M., Morton, P.L., Nenes, A., Mihalopoulos, N., Violaki, K., Gao, Y., Sahai, S., Castorina, E., 2018. Enhanced iron solubility at low pH in global aerosols. Atmosphere (Basel) 9 (201). https://doi.org/10.3390/atmos9050201.
- Jackson, G.A., Burd, A.B., 2015. Simulating aggregate dynamics in ocean biogeochemical models. Prog. Oceanogr. 133, 55–65. https://doi.org/10.1016/j.pocean.2014.08.
- Journet, E., Desboeufs, K.V., Caquineau, S., Colin, J.L., 2008. Mineralogy as a critical factor of dust iron solubility. Geophys. Res. Lett. 35, L07805. https://doi.org/10. 1029/2007GL031589.
- Kandler, K., Benker, N., Bundke, U., Cuevas, E., Ebert, M., Knippertz, P., Rodríguez, S., Schütz, L., Weinbruch, S., 2007. Chemical composition and complex refractive index of Saharan Mineral Dust at Izaña, Tenerife (Spain) derived by electron microscopy. Atmos. Environ. 41, 8058–8074. https://doi.org/10.1016/j.atmosenv.2007.06.047.
- Krueger, B.J., Grassian, V.H., Cowin, J.P., Laskin, A., 2004. Heterogeneous chemistry of individual mineral dust particles from different dust source regions: the importance of particle mineralogy. Atmos. Environ. https://doi.org/10.1016/j.atmosenv.2004. 07.010
- Lohmann, U., Quaas, J., Kinne, S., Feichter, J., 2007. Different approaches for constraining global climate models of the anthropogenic indirect aerosol effect. Bull. Am. Meteorol. Soc. 243–249. https://doi.org/10.1175/BAMS-88-2-243.
- Lu, W., Zhao, W., Balsam, W., Lu, H., Liu, P., Lu, Z., Ji, J., 2017. Iron mineralogy and speciation in clay-sized fractions of Chinese Desert sediments. J. Geophys. Res.

- Atmos. 122, 13,458-13,471. https://doi.org/10.1002/2017JD027733.
- Ma, X., Lin, B.K., Wei, X., Kniep, J., Lin, Y.S., 2013 Gamma-Alumina Supported Carbon Molecular Sieve Membrane for Propylene/Propane Separation. n.d.https://doi.org/ 10.1021/ie303188c.
- Mallampati, S.R., Lee, B.H., Mitoma, Y., Simion, C., 2018. Sustainable recovery of precious metals from end-of-life vehicles shredder residue by a novel hybrid ball-milling and nanoparticles enabled froth flotation process. J. Clean. Prod. https://doi.org/10.1016/j.jclepro.2017.09.279.
- Nakamura, R., Nakato, Y., 2004. Primary intermediates of oxygen photoevolution reaction on TiO₂ (rutile) particles, revealed by in situ FTIR absorption and photoluminescence measurements. J. Am. Chem. Soc. 126, 1290–1298. https://doi.org/10.1021/ija0388764
- Nanayakkara, C.E., Jayaweera, P.M., Rubasinghege, G., Baltrusaitis, J., Grassian, V.H., 2014. Surface photochemistry of adsorbed nitrate: the role of adsorbed water in the formation of reduced nitrogen species on alpha-Fe₂O₃ particle surfaces. J. Phys. Chem. A 118, 158–166. https://doi.org/10.1021/jp409017m.
- Nenes, A., Krom, M.D., Mihalopoulos, N., Van Cappellen, P., Shi, Z., Bougiatioti, A., Zarmpas, P., Herut, B., 2011. Atmospheric acidification of mineral aerosols: a source of bioavailable phosphorus for the oceans. Atmos. Chem. Phys. https://doi.org/10. 5194/acp-11-6265-2011.
- Paris, R., Desboeufs, K.V., Journet, E., 2011. Variability of dust iron solubility in atmospheric waters: investigation of the role of oxalate organic complexation. Atmos. Environ. https://doi.org/10.1016/j.atmosenv.2011.08.068.
- Ravelo-Pérez, L.M., Rodríguez, S., Galindo, L., García, M.I., Alastuey, A., López-Solano, J., 2016. Soluble iron dust export in the high altitude saharan air layer. Atmos. Environ. https://doi.org/10.1016/j.atmosenv.2016.03.030.
- Reynolds, R.L., Cattle, S.R., Moskowitz, B.M., Goldstein, H.L., Yauk, K., Flagg, C.B., Berquó, T.S., Kokaly, R.F., Morman, S., Breit, G.N., 2014. Iron oxide minerals in dust of the Red Dawn event in eastern Australia, September 2009. Aeolian Res. https:// doi.org/10.1016/j.aeolia.2014.02.003.
- Rubasinghege, G., Kyei, P.K., Scherer, M.M., Grassian, V.H., 2012. Proton-promoted dissolution of α-FeOOH nanorods and microrods: size dependence, anion effects (carbonate and phosphate), aggregation and surface adsorption. J. Colloid Interface Sci. 385, 15–23. https://doi.org/10.1016/j.jcis.2012.06.049.
- Rubasinghege, G., Lentz, R.W., Scherer, M.M., Grassian, V.H., Finlayson-Pitts, B.J., 2010. Simulated atmospheric processing of iron oxyhydroxide minerals at low pH: roles of particle size and acid anion in iron dissolution. Proc. Natl. Acad. Sci. Unit. States Am. 107, 6628–6633. https://doi.org/10.1073/pnas.0910809107.
- Sarkar, D., 2005. Physical and Chemical Methods in Soil Analysis.
- Shao, L.Y., Li, W.J., Yang, S.S., Shi, Z.B., Lü, S.L., 2007. Mineralogical characteristics of airborne particles collected in Beijing during a severe Asian dust storm period in spring 2002. Sci. China Earth Sci. 50, 953–956. https://doi.org/10.1007/s11430-007-0035-7
- Shkrob, I.A., Marin, T.W., Chemerisov, S.D., Wishart, J.F., 2011. Radiation and radical chemistry of NO₃⁻, HNO₃, and dialkylphosphoric acids in room-temperature ionic liquids. J. Phys. Chem. B 115, 10927–10942. https://doi.org/10.1021/jp206579j.
- Silveira, J.E., Paz, W.S., Garcia-Muñoz, P., Zazo, J.A., Casas, J.A., 2017. Uv-led/ilmenite/persulfate for azo dye mineralization: the role of sulfate in the catalyst deactivation. Appl. Catal. B Environ. 219, 314–321. https://doi.org/10.1016/j.apcatb.2017.07.072
- Stucki, J.W., 1981. The quantitative assay of minerals for ${\rm Fe}^{2+}$ and ${\rm Fe}^{3+}$ using 1,10-phenanthroline; sources of variability. Soil Sci. Soc. Am. J. 45, 638–641.
- Tabesh, S., Davar, F., Loghman-Estarki, M.R., 2018. Preparation of γ-Al2O3nanoparticles using modified sol-gel method and its use for the adsorption of lead and cadmium ions. J. Alloy. Comp. https://doi.org/10.1016/j.jallcom.2017.09.246.
- Wiederhold, J.G., Kraemer, S.M., Teutsch, N., Borer, P.M., Halliday, A.N., Kretzschmar, R., 2006. Iron isotope fractionation during proton-promoted, ligand-controlled, and reductive dissolution of goethite. Environ. Sci. Technol. 40, 3787–3793. https://doi. org/10.1021/es052228v.
- Wijenayaka, L.A., Rubasinghege, G., Baltrusaitis, J., Grassian, V.H., 2012. Surface chemistry of α-FeOOH nanorods and microrods with gas-phase nitric acid and water vapor: insights into the role of particle size, surface structure, and surface hydroxyl groups in the adsorption and reactivity of α-FeOOH with atmospheric gases. J. Phys. Chem. C. 116. 12566–12577. https://doi.org/10.1021/jij301139x.
- Chem. C 116, 12566–12577. https://doi.org/10.1021/jp301139x.

 Xiong, L. Bin, Li, J.L., Yang, B., Yu, Y., 2012. Ti³⁺ in the surface of titanium dioxide: generation, properties and photocatalytic application. J. Nanomater. 1–13. https://doi.org/10.1155/2012/831524.
- Yamashita, T., Hayes, P., 2008. Analysis of XPS spectra of Fe²⁺ and Fe³⁺ ions in oxide materials. Appl. Surf. Sci. 254, 2441–2449. https://doi.org/10.1016/j.apsusc.2007. 09.063.
- Zhao, Y., Zou, X., Gao, J., Wang, C., Li, Y., Yao, Y., Zhao, W., Xu, M., 2018. Clay mineralogy and source-to-sink transport processes of Changjiang River sediments in the estuarine and inner shelf areas of the East China Sea. J. Asian Earth Sci. 152, 91–102. https://doi.org/10.1016/j.jseaes.2017.11.038.

Supporting Information

Iron Dissolution and Speciation in Atmospheric Mineral Dust: Metal-Metal Synergistic and Antagonistic Effects

Content

| 1. Electrical Conductivity (EC) Measurements and Ionic Strength (I) Calculations | 2 |
|--|----|
| 1.1. Electrical Conductivity Measurements | 2 |
| 1.2. Calculation of Ionic Strength of the Solutions | 2 |
| 2. Pseudo First-Order Rates of Iron Production | 5 |
| 3. [Fe(II)]/[Total Fe] Production | 6 |
| 4. pH Variations Over Time | 7 |
| 5. Mössbauer Spectroscopy and Magnetization Measurements | 8 |
| 6. References | 11 |

1. Electrical Conductivity (EC) Measurements and Ionic Strength (I) Calculations

1.1. Electrical Conductivity Measurements

The experimentally determined EC of the solutions before and after the additions of the minerals can be used to infer the initial reactions prone to happen in the solution. The measured ECs for the current study are given in **Table S1**. Addition of minerals, α-Fe₂O₃, TiO₂ or Al₂O₃ decreased the EC slightly, suggesting the surface adsorption of ions and thereby the reduction of the amount of the charged species remaining in the solution. Comparatively larger decrease of EC in hematite with Al₂O₃ indicates the high adsorption capacity of alumina. The addition of CaO to hematite increases the EC of the solution, suggesting that the reaction of CaO with water and nitric acid yields dissolved ions as provided in **Equations S1**.

Overall reaction,

$$CaO_{(s)} + 2HNO_{3(aq)} \rightarrow Ca^{2+}_{(aq)} + 2NO_{3}^{-}_{(aq)} + H_2O_{(l)}$$
 Equation S1

At the 48th hour, as expected due to the dissolution of minerals, the conductivity of each solution increased but to different extents.

Table S1. The measured electrical conductivities of the solutions before and after the addition of minerals

| Sample | Electrical Conductivity (mS cm ⁻¹) | | | |
|--|--|-------------------|--|--|
| • | Initial (After addition) | Final (48th hour) | | |
| pH 2 HNO ₃ (N ₂ purged, no minerals added) | 3.84±0.04 | N/A | | |
| α -Fe ₂ O ₃ | 3.62 ± 0.05 | 4.06 ± 0.08 | | |
| α-Fe ₂ O ₃ :TiO ₂ | 3.64 ± 0.04 | 4.38 ± 0.10 | | |
| α-Fe ₂ O ₃ :Al ₂ O ₃ | 3.56 ± 0.07 | 3.75 ± 0.08 | | |
| α-Fe ₂ O ₃ :CaO | 3.91 ± 0.05 | 4.22 ± 0.07 | | |

1.2. Calculation of Ionic Strength of the Solutions

Electrical conductivity is a good indicator in determining ionic strength of the solutions. [Sarojini et al., 2013] The ionic strengths were calculated using the relation established by Griffin and Jurinak, which has been adopted by many researchers thereafter. [Sarkar, 2005; Chesworth, 2008]

The relation between experimentally determined EC and the solution ionic strength is given in the **Equation S2** below.

$$I \text{ (mol } L^{-1}) = 0.0127 \text{ EC (mS cm}^{-1})$$
 Equation S2

The calculated ionic strengths are given in **Table S2**.

Table S2. The calculated ionic strengths of solutions after the addition of minerals and at the $48^{\rm th}$ hour

| Sample | Ionic strength (mol L ⁻¹) x 10 ⁻⁴ | | | |
|--|--|-------------------------------|--|--|
| | Initial (After addition) | Final (48 th hour) | | |
| α-Fe ₂ O ₃ | 460±6.35 | 520±10.2 | | |
| α-Fe ₂ O ₃ :TiO ₂ | 460±5.13 | 560±12.7 | | |
| α-Fe ₂ O ₃ :Al ₂ O ₃ | 450±8.92 | 480±10.2 | | |
| α-Fe ₂ O ₃ :CaO | 500±5.73 | 540±8.89 | | |

The mass normalized dissolved iron concentrations that are normalized to ionic strength are given below in **Figure S1-S2**. First, all the ionic strength values were normalized to highest observed ionic strength, i.e., 0.050 mol L⁻¹ for α -Fe₂O₃:CaO solution, by multiplying a factor of 'x' where x = 25/23 for hematite and hematite with TiO₂ solutions and 10/9 for hematite with Al₂O₃ solution.

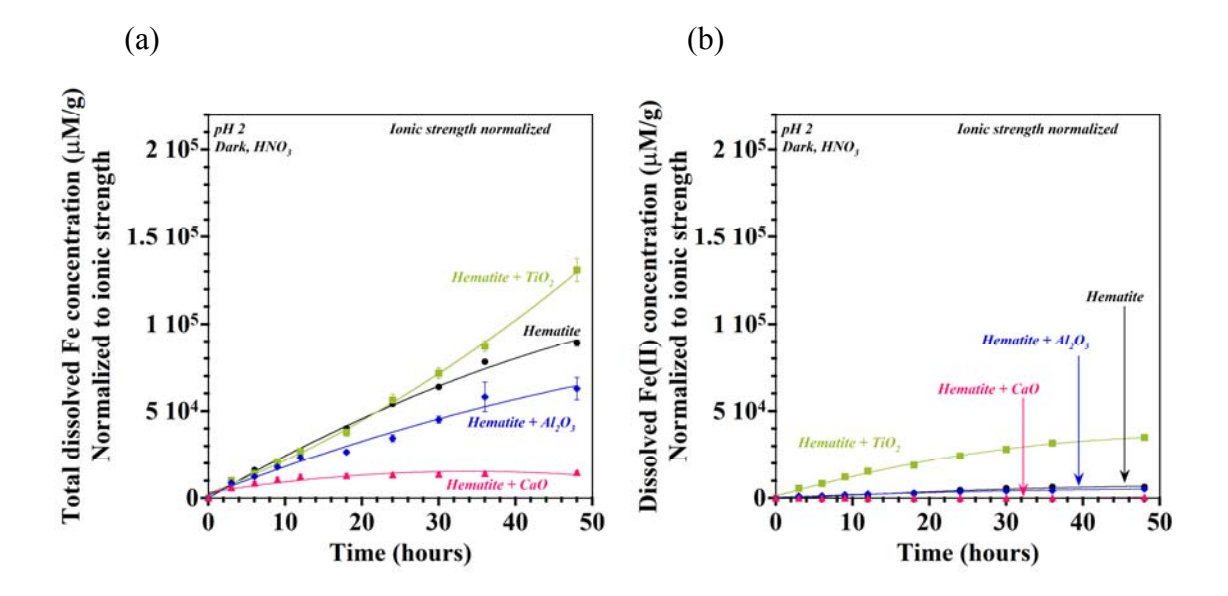


Figure S1. The ionic strength normalized dissolutions of iron from hematite, hematite + TiO₂, hematite + Al₂O₃ and hematite + CaO (a) total iron dissolution, (b) dissolved Fe(II) concentration in the presence of pH 2 nitric acid in dark.

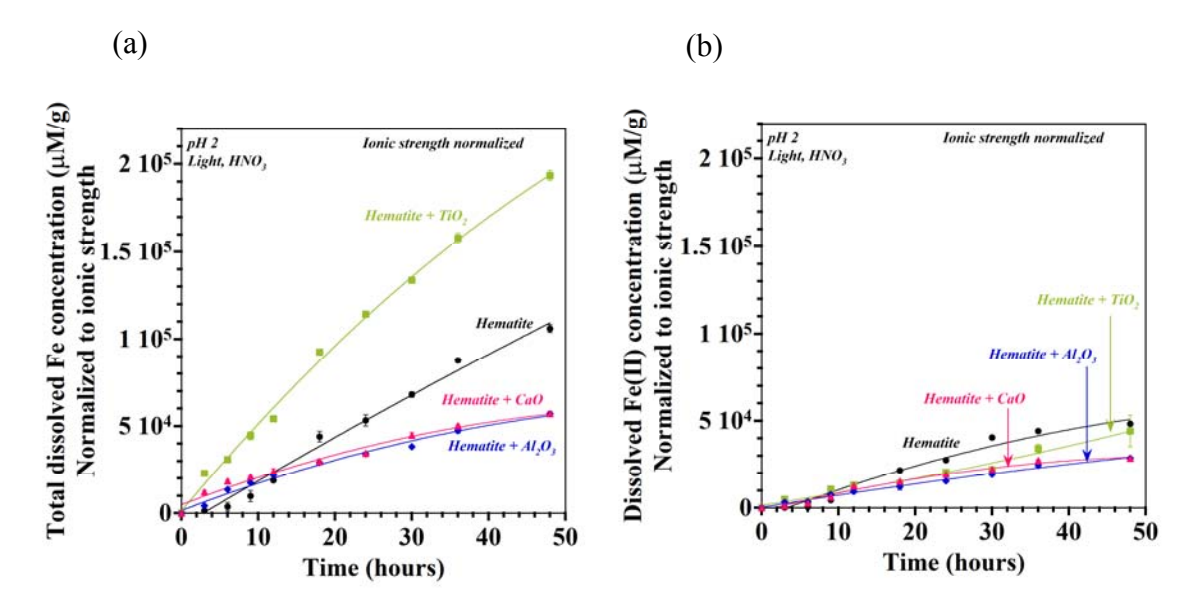


Figure S2. The ionic strength normalized dissolutions of iron from hematite, hematite $+ \operatorname{TiO}_2$, hematite $+ \operatorname{Al}_2\operatorname{O}_3$ and hematite $+ \operatorname{CaO}$ (a) total iron dissolution, (b) dissolved Fe(II) concentration in the presence of pH 2 nitric acid in light.

2. Pseudo First-Order Rates of Iron Production

The pseudo first-order rates of iron production are provided in **Table S3**. The rates were calculated using Langmuir isotherm and by linear regression for the results from the first 18 hours.

Table S3. The pseudo first-order rates of iron production in dark and light conditions at pH 2 nitric acid for mineral dust proxies

| Sample | Pseudo first-order rate (μM g ⁻¹ hr ⁻¹) | | | | |
|---|--|----------|----------|----------|--|
| | Total | Fe(II) | | | |
| | Dark | Light | Dark | Light | |
| α-Fe ₂ O ₃ | 117±3.2 | 106±2.5 | 9.95±1.2 | 44.1±3.1 | |
| α-Fe ₂ O ₃ : TiO ₂ | 115±2.0 | 200±1.7 | 54.2±2.1 | 63.4±1.2 | |
| α-Fe ₂ O ₃ : Al ₂ O ₃ | 82.0±2.4 | 76.5±1.9 | 23.7±1.4 | 46.3±1.6 | |
| α-Fe ₂ O ₃ : CaO | 30.2±1.4 | 77.8±2.6 | 0 | 47.2±2.0 | |

Table S4. The pseudo first-order rates of total iron dissolution from natural dust samples in mass normalized basis (μ M g⁻¹) and surface area normalized basis (μ Mm²). Surface area normalized rates are given in the parenthesis.

| Sample | Pseudo first-order rate of total iron production | | | |
|--------|--|-----------------|--|--|
| | Dark | Light | | |
| SZ1 | 55±3 | 75±5 | | |
| | (7±0.4) | (9±1) | | |
| RO | 20±2 | 14±3 | | |
| | (0.35 ± 0.04) | (0.25 ± 0.05) | | |

3. [Fe(II)]/[Total Fe] Production

The percent Fe(II) production is provided in **Table S4.** The percent Fe(II) production was calculated at the end of the 48th hour.

Table S5. The [Fe(II)]/[Total Fe] production from each reaction medium at pH 2 nitric acid

| Sample | [Fe(II)]/[Total Fe] % | | | |
|---|-----------------------|-------|--|--|
| | Dark | Light | | |
| α-Fe ₂ O ₃ | 7.0 | 45 | | |
| α-Fe ₂ O ₃ : TiO ₂ | 27 | 23 | | |
| α-Fe ₂ O ₃ : Al ₂ O ₃ | 9.0 | 49 | | |
| α-Fe ₂ O ₃ : CaO | 3.0 | 49 | | |
| SZ1 | 51 | 27 | | |
| RO | 40 | 73 | | |

4. pH Variations Over Time

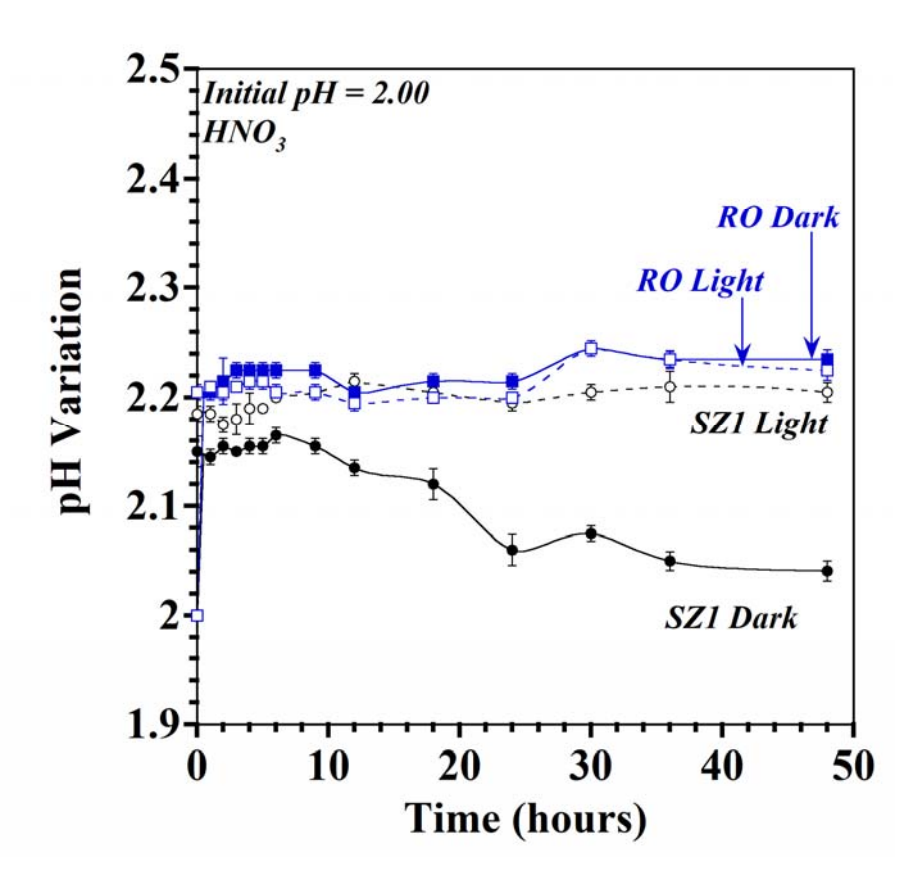


Figure S3. The variation of pH over time in the two mineral dusts SZ1 and RO systems in dark and light conditions

5. Mössbauer Spectroscopy and Magnetization Measurements

To further characterize the distribution of Fe among mineral phases in the natural dust samples, Mössbauer spectroscopy and magnetic investigations were carried out on powdered samples (~100 mg) at the Institute for Rock Magnetism (IRM), University of Minnesota, USA. Measurements were made at 300 K and 4.2 K using a constant-acceleration spectrometer equipped with a Nitrogen shielded Helium dewar. Spectra were collected in transmission geometry with a ⁵⁷Co/Rh source. An alpha-Fe foil at room temperature was used to calibrate isomer shifts and velocity scale. Mössbauer spectra were fit using the NORMOS program (Brand, 1987) providing estimates for the hyperfine field (Bhf), isomer shift (IS), and quadrupole splitting (QS) for each subspectra. Magnetically split sextet subspectra were fit using a distribution of hyperfine-fields (HFD). Uncertainties for Mössbauer parameters are ±0.01 mm/s for IS and QS, ±0.1 T for Bhf., and ±5% for spectral area.

Room temperature hysteresis loops were obtained in a vibrating sample magnetometer (Princeton Corporation Measurements) using an electromagnet to produce fields up to 1 T. Hysteresis parameters (saturation magnetization, M_s ; saturation remanence, M_r ; coercivity, B_c ; and high-field susceptibility, c_{hf}) were determined from loops after high-field slope correction (Jackson and Solheid, 2010). The concentration of all iron oxide minerals is reflected by values of saturation magnetization (M_s), but is primarily generated by ferrimagnetic minerals with high intrinsic M_s (e.g., magnetite or maghemite). The magnetite weight-percent was determined from the room-temperature bulk M_s values and the known value for pure magnetite (M_s =92 Am2/kg) as follows: Magnetite wt% = 100% (M_s)_{bulk}/92

Table S6: Saturation magnetization for natural dust samples

| ID | M _s (Am ² /kg) | Magnetite wt% | % of Total Fe |
|-----|--------------------------------------|---------------|---------------|
| RO | 0.0521 | 0.06 | 0.90 |
| SZ1 | 0.0947 | 0.10 | 1.50 |

Table S7. Mössbauer parameters at 300 K and 4.2 K for natural dust samples

| IDBhf(T) | | T = 300 K | | | T = 4.2 K | | | | |
|----------|---------|---------------------------|---------------------------|--------------|-----------|--------------|--------------|----|-------------|
| | Bhf(T)a | QS (mm/s) ^b | IS (mm/s) ^c | 0∕0 d | Bhf(T) | QS (mm/s) | IS (mm/s) | % | Assignmente |
| RO | 50 | -0.16 | 0.33 | 15 | 52.2 | -0.17 | 0.51 | 43 | hematite |
| | | 0.39 | 0.37 | 50 | | 0.39 | 0.49 | 35 | Fe(III) |
| | | 0.90 | 0.37 | 30 | | 0.94 | 0.49 | 18 | Fe(III) |
| | | 2.79 | 1.02 | 5 | | 2.8 | 0.94 | 4 | Fe(II) |
| SZ1 | 51.1 | -0.21 | 0.41 | 37 | 52.6 | -0.13 | 0.47 | 52 | hematite |
| | | 0.47 | 0.51 | 36 | | 0.38 | 0.55 | 20 | Fe(III) |
| | | 1.53 | 0.63 | 21 | | 1.17 | 0.59 | 17 | Fe(III) |
| | | 3.09 | 0.97 | 6 | | 3.06 | 1.13 | 11 | Fe(II) |

^a B_{hf} , mean value of the hyperfine field distribution hyperfine field; uncertainties are $\pm 0.1~T$

 $^{^{}b}$ QS quadrupole splitting; uncertainties are ± 0.01 mm/s.

^c IS isomer shift; uncertainties are ± 0.01 mm/s.

^d %, relative proportion of subspectrum to total area; uncertainties are±5% for spectral areas.

^e Phase, iron oxide mineral or form of iron indicated by Fe(III) and Fe(II) doublets that correspond to paramagnetic iron in multiple components with overlapping doublets having similar IS and QS values, such as phyllosilicates and nanophase ferric oxides. Such overlap precludes firm mineral identification of these iron phases. Results for RO are from Reynolds et al [2014]

6. References

Chesworth, W., 2008. Encyclopedia of Soil Science.

Sarkar, D., 2005. Physical and Chemical Methods in Soil Analysis.

Sarojini, K.G.K., Manoj, S. V., Singh, P.K., Pradeep, T., Das, S.K., 2013. Electrical Conductivity of Ceramic and Metallic Nanofluids. Colloids Surfaces A Physicochem. Eng. Asp. 417, 39–46. https://doi.org/10.1016/j.colsurfa.2012.10.010